Mirror instability and L-mode electromagnetic ion cyclotron instability: Competition in the Earth's magnetosheath

Masafumi Shoji, Yoshiharu Omura, Bruce T. Tsurutani, Olga P. Verkhoglyadova, Bertrand Lembège

Mirror instability and L-mode electromagnetic ion cyclotron instability: Competition in the Earth's magnetosheath

Masafumi Shoji,[1] Yoshiharu Omura,[1] Bruce T. Tsurutani,[2] Olga P. Verkhoglyadova,[2] and Bertrand Lembege[1,3]

Received 31 December 2008; revised 1 July 2009; accepted 17 July 2009; published 9 October 2009.

[1] We performed both two- and three-dimensional hybrid simulations of the competing processes between the L-mode electromagnetic ion cyclotron (EMIC) and mirror instabilities, assuming anisotropic energetic ions with $T_\perp/T_\parallel = 4.0$. In the two-dimensional model, the energy of the EMIC waves is higher at the linear growth phase because its growth rate is larger than that of the mirror mode. In the three-dimensional model, however, the energy of the mirror mode waves is larger than that of the EMIC waves for all times because the wave number spectra of mirror mode waves form torus-like structures. We also theoretically derived a necessary condition for the dominance of the mirror instability. As the mirror mode waves relax the temperature anisotropy effectively, the linear growth rates of the EMIC waves become smaller before saturation. The EMIC waves cause heating of protons trapped by the nonlinear potentials due to coexistence of forward and backward propagating waves and inverse cascading. They terminate the linear growth of EMIC waves. Because of these parallel heatings, the temperature anisotropy decreases to the threshold of the mirror instability and thus the mirror mode wave saturates. At the nonlinear stage, coalescence of the mirror mode waves takes place in both models. The quick dissipation of the EMIC waves occurs due to the heating by the nonlinear processes. On the other hand, the coalescence is a much slower process than the nonlinear processes of EMIC waves, and thus the mirror mode waves remain in the three-dimensional model.

Citation: Shoji, M., Y. Omura, B. T. Tsurutani, O. P. Verkhoglyadova, and B. Lembege (2009), Mirror instability and L-mode electromagnetic ion cyclotron instability: Competition in the Earth's magnetosheath, *J. Geophys. Res.*, *114*, A10203, doi:10.1029/2008JA014038.

1. Introduction

[2] Large perpendicular-to-parallel ion temperature anisotropy ratios ($T_\perp/T_\parallel > 1$) can be expected in two regions of planetary magnetosheaths: downstream of the quasiperpendicular portion of the bow shocks (see Figure 1) and close to the magnetopause where field-line draping effects are important [*Midgeley and Davis*, 1963; *Zwan and Wolf*, 1976]. In the former region, preferential plasma heating in $T_\perp$ takes place due to shock compression [*Kennel et al.*, 1985], and in the second region the anisotropy is caused by flow of plasma with high $V_\parallel$ out the ends of the magnetic flux tubes.

[3] These ion anisotropies can lead to two different instabilities, the mirror mode [*Chandrasekhar et al.*, 1958; *Hasegawa*, 1969, 1975] and the electromagnetic ion cyclotron (EMIC) instability [*Kennel and Petschek*, 1966]. Of the two instabilities, it has been suggested by *Lacombe and Belmont* [1995] the L-mode EMIC instability is dominant for low ion betas whereas the mirror mode is dominant for high ion betas. With ISEE-1 and -2 magnetic field and plasma data, *Tsurutani et al.* [1982] first established the existence of the mirror mode in the magnetosheath of the Earth, and with Pioneer 10 and 11 magnetic field data, in the magnetosheaths of Jupiter and Saturn.

[4] Since the initial confirmation of the existence of mirror modes in the Earth's magnetosheath, they have been observed throughout the heliosphere. They have been detected at comets Giacobini-Zinner [*Tsurutani et al.*, 1999] and Halley [*Russell et al.*, 1989; *Glassmeier et al.*, 2003] as well as in interplanetary space proper [*Tsurutani et al.*, 1992]. More recent confirmatory magnetosheath observations at Earth are found in the works of *Tsurutani et al.* [1984], *Hubert* [1994], *Phan et al.* [1994], and *Lacombe and Belmont* [1995], at Jupiter and Saturn are in the works of *Tsurutani et al.* [1993], *Bavassano et al.* [1998], *Violante et al.* [1995], and *Erdos and Balogh* [1996]. These observations that mirror modes are often dominant coherent magnetic structures in planetary magnetosheaths even for low beta plasmas is a long-standing puzzle in space plasmas.

[1] Research Institute of Sustainable Humanosphere, Kyoto University, Uji, Japan.
[2] Jet Propulsion Laboratory, California Institute of Technology, Pasadena, California, USA.
[3] LATMOS-UVSQ-IPSL-CNRS, Velizy, France.

0148-0227/09/2008JA014038

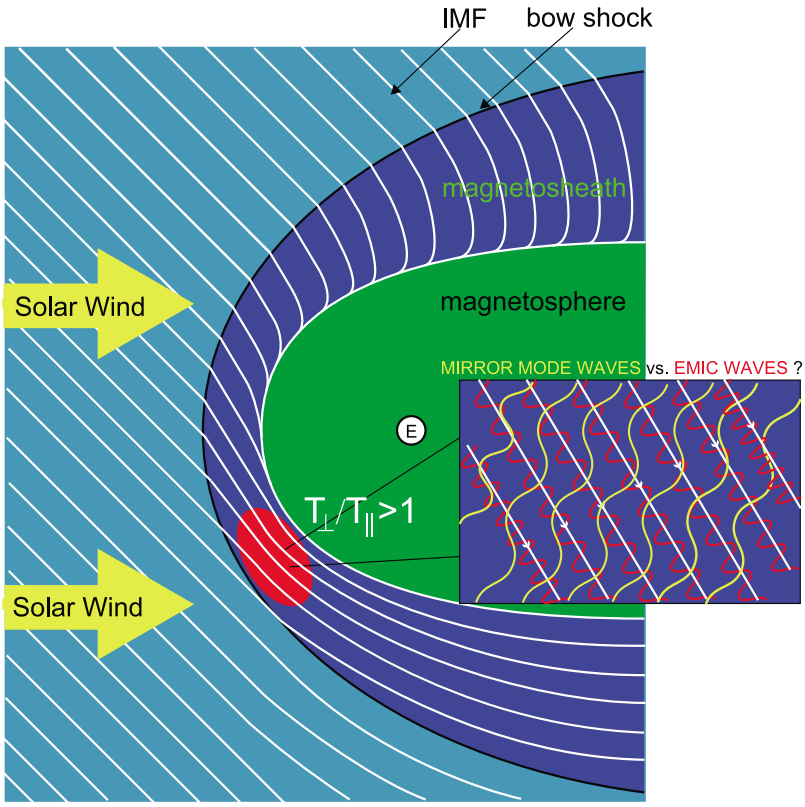

Figure 1. A schematic illustration of the magnetosphere of the Earth. The white lines show the interplanetary magnetic field (IMF).

[5] The presence of He^{++} tends to increase the EMIC threshold [*Price et al.*, 1986]. On the other hand, the mirror mode growth is less affected by the presence of He^{++} ions [*Brinca and Tsurutani*, 1989]. Thus *Gary* [1992] and *Gary et al.* [1993] have argued that this mechanism of lowering the EMIC linear growth rate is a possible cause of mirror mode formation and domination in planetary magnetosheaths.

[6] The purpose of this paper is to try another approach to the problem. In section 2, we perform linear analysis of the linear growth rate of each instability. We show that the linear growth rate of the EMIC modes is indeed higher than that of the mirror mode, in agreement with previously published results. In section 3, using two-dimensional and three-dimensional hybrid codes, we compare wave energy growth rates of both the mirror and EMIC modes. In both cases, only a hydrogen plasma is assumed, removing any possible ambiguities associated with multiple ion effects. The results indicate a principal difference between two-dimensional and three-dimensional approaches and show that the free energy flows mostly into the mirror mode.

2. Linear Analysis

[7] We calculate theoretical growth rates of instabilities by solving the kinetic plasma dispersion relation $H(\boldsymbol{k}, \omega) = 0$, where $\boldsymbol{k}$ is a wave number vector consisting of orthogonal components $k_{\|}$ and $k_{\perp}$ (parallel and perpendicular to the ambient magnetic field), and ω is a complex frequency of each mode. The imaginary part of ω is the linear growth rate. We assume bi-Maxwellian velocity distributions as functions of $v_{\|}$ and $v_{\perp}$, parallel and perpendicular to the static magnetic field, respectively, for H^{+} defined by

$$f_{\mathrm{H}}(v_{\|}, v_{\perp}) = \frac{n_{\mathrm{H}}}{(2\pi)^{3/2} V_{\|\mathrm{H}} V_{\perp\mathrm{H}}^2} \exp\left(-\frac{v_{\|}^2}{2V_{\|\mathrm{H}}^2} - \frac{v_{\perp}^2}{2V_{\perp\mathrm{H}}^2}\right), \quad (1)$$

where n_{H} is the density of protons. The thermal velocities of ions are given by $V_{\|\mathrm{H}} = \sqrt{\frac{T_{\|\mathrm{H}}}{m_{\mathrm{H}}}}$, $V_{\perp\mathrm{H}} = \sqrt{\frac{T_{\perp\mathrm{H}}}{m_{\mathrm{H}}}}$, where $T_{\|\mathrm{H}}$ and $T_{\perp\mathrm{H}}$ are temperatures of the protons in the parallel and perpendicular directions, respectively, and m_{H} is the mass of proton. The plasma frequency of proton is $\omega_{\mathrm{pH}} = 300\Omega_{\mathrm{H}}$, where Ω_{H} is the cyclotron frequency of protons. The temperature anisotropy of ions is varied over the range of $2.5 \leq T_{\perp\mathrm{H}}/T_{\|\mathrm{H}} \leq 4.0$ and the different ion beta values of protons are 0.5, 1.0 or 2.5. We assume the electron beta value βe = 1.0.

[8] The top panels of Figure 2 show the ω-$k_{\|}$ diagrams of the L-mode EMIC waves (dashed line) and the mirror mode waves (solid line) for different ion β values (2.5, 1.0 and 0.5). The middle panels show the growth rate of each mode for a temperature anisotropy of ions $T_{\perp}/T_{\|} = 4.0$. The bottom panels show the maximum growth rate of each mode for various temperature anisotropies. In all cases, the maximum growth rate of L-mode EMIC waves is higher than that of mirror mode wave. Therefore, the fastest growing mode of the EMIC instability can initially grow faster than that of the mirror instability driven by the temperature anisotropy. We note that, however, the growth

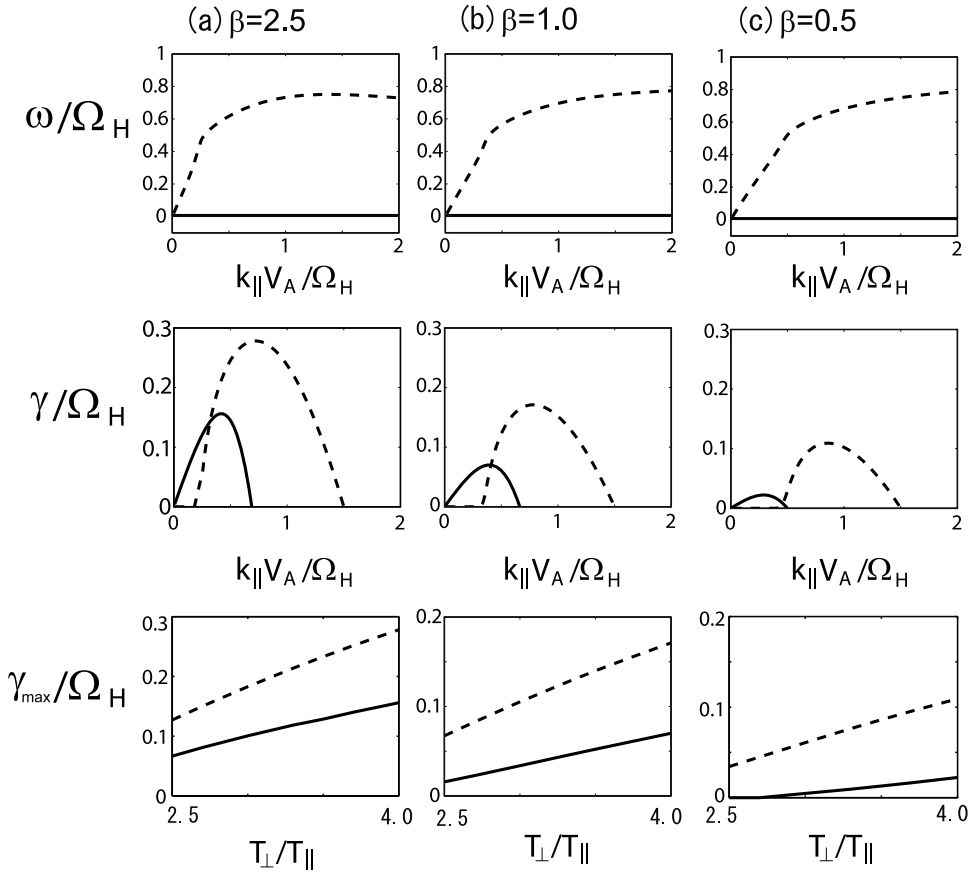

Figure 2. The linear analysis of each mode. The top panels show the ω-k diagram of the L-mode EMIC waves (dashed line) and the mirror mode waves (solid line) for different ion β. The middle panels show the growth rate of each mode. The temperature anisotropy of ions in these panels is 4.0. The bottom panels show the maximum growth rate of each mode as a function of the temperature anisotropy for a constant value β.

rate does not correspond directly to the increase of the total energy of each mode.

3. Hybrid Simulation

[9] We analyze the competing process between the L-mode EMIC and mirror instabilities using a three-dimensional hybrid code for three models: one-dimensional, two-dimensional, and three-dimensional physical models.

3.1. Basic Equations and Parameters

[10] The basic equations of the hybrid code are given as follows:

$$\nabla \times \boldsymbol{E} = -\frac{\partial \boldsymbol{B}}{\partial t}, \tag{2}$$

$$\nabla \times \boldsymbol{B} = \mu_0 \boldsymbol{J}, \tag{3}$$

$$-en_e\boldsymbol{E} + \boldsymbol{J}_e \times \boldsymbol{B} - \nabla p_e = 0, \tag{4}$$

$$\frac{d\boldsymbol{v}_H}{dt} = \frac{q_H}{m_H}(\boldsymbol{E} + \boldsymbol{v}_H \times \boldsymbol{B}), \tag{5}$$

where $\boldsymbol{E}$ is the electric field, $\boldsymbol{B}$ is the magnetic field, μ_0 is the magnetic permeability in vacuum, and $\boldsymbol{J}$ is the current density. We have neglected the displacement current.

[11] Equation (4) shows the momentum equation of the electron fluid, in which the inertia of the electron fluid has been neglected. The value $-e$ is the charge of an electron and $\boldsymbol{J}_e$ and p_e are the current and pressure of electrons, respectively. The current of the electron fluid is given by

$$\boldsymbol{J}_e = \boldsymbol{J} - q_H n_H \boldsymbol{v}_H. \tag{6}$$

We assume adiabatic variations of the electron pressure p_e:

$$p_e = p_{e0}(n_e/n_0)^\gamma, \tag{7}$$

where p_{e0} and n_0 are the initial pressure and density of electrons, respectively, and γ is the ratio of specific heat. The charge density of electrons is given by the quasineutrality condition. Equation (5) shows the equation of motion of protons, where v_H, q_H, m_H are the velocity, charge, and mass of protons.

[12] In this hybrid code, the Current Advance Method and the Cyclic Leapfrog (CAM-CL) modified by Buneman-Boris method [*Matsumoto and Omura*, 1993] are used to

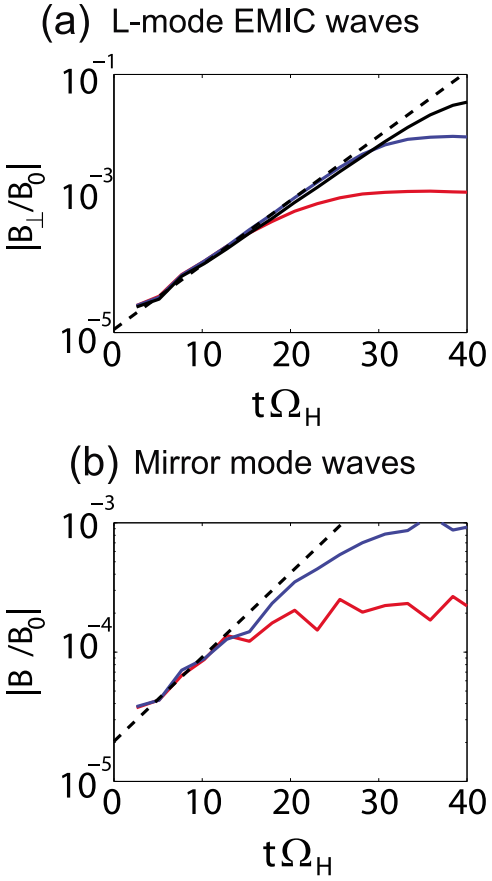

Figure 3. (a) The effect of mirror instability on the saturation levels of the L-mode EMIC waves at $m_x = 41$, $m_y = 1$, $m_z = 1$. (b) The saturation levels of the mirror mode waves at $m_x = 33$, $m_y = 40$, $m_z = 1$. In each panel, the black, blue, and red lines show the saturation level in the one-dimensional, two-dimensional, and three-dimensional models, respectively, and the dashed black lines show the theoretical growth rate of each mode at the initial phase.

calculate the equation of motion of ions. For computing the ion current in each grid, we used the "area sharing method" to improve the accuracy. Moreover, the three-point digital filter [*Birdsall and Langdon*, 1985] is applied to suppress current noise that can arise in high wave number space caused by a lack of particles.

[13] The bi-Maxwellian protons are uniformly distributed in the simulation space. The number of superparticles in the simulation is $N_p = 2^{31}$, the charge to mass ratio is $q_s/m_s = 1.0$, the plasma frequency of proton is $\omega_{pH}/\Omega_H = 300$. The thermal speeds of protons in the parallel and perpendicular directions are $V_{\|H}/V_A = 0.707$ and $V_{\perp H}/V_A = 1.414$, respectively, where V_A is the Alfven velocity of protons. Thus the temperature anisotropy is $T_\perp/T_\| = 4.0$ and the ion beta in the parallel direction is $\beta_{\|H} = \frac{nmV_{\|H}^2/2}{B_0^2/(2\mu_0)} = 0.50$, where μ_0 is the permeability in vacuum. The maximum growth rate of the L-mode EMIC instability and the mirror instability is then 0.28 and 0.16 as shown in Figure 2, respectively. These ion parameters are the same in the three different simulation models. In the Earth's magnetosheath, the temperature anisotropy and beta value of ions are inversely correlated in the range of $1.2 \le T_\perp/T_\| \le 5.0$ and $0.01 \le \beta_\| \le 10.0$ because of the regulation of the EMIC instability [*Fuselier et al.*, 1994]. These observations represents the results of the instability. In this study, we analyze the instabilities driven by the fresh injection of the anisotropic protons. Thus we initially assume a strong temperature anisotropy and a high beta value in a possible range of observation to drive both L-mode EMIC and mirror instabilities.

[14] A constant background magnetic field $\boldsymbol{B}_0$ is assumed in the x direction. The electron beta is $\beta_e = 1.0$. The grid spacing Δx is $1.0V_A/\Omega_H$. The numbers of grid points ($n_x \times n_y$ $n_y \times n_z$) are $512 \times 512 \times 512$, $512 \times 512 \times 1$, and $512 \times 1 \times 1$ in the three-dimensional, two-dimensional, and one-dimensional models, respectively. The number of time steps is 3200 with $\Delta t = 0.04/\Omega_H$. Periodic boundary is used in each dimension.

3.2. Linear Stage Competition Between Mirror and L-Mode EMIC Instabilities

[15] Figures 3a and 3b show the time histories of the L-mode EMIC waves and the mirror mode waves at $m_x = 41$, $m_y = 1$, $m_z = 1$ and $m_x = 33$, $m_y = 40$, $m_z = 1$, respectively, where m_j ($j = x, y, z$) is the mode number in each direction. The growth rates of each wave have good agreement with those given by the kinetic linear theories (dashed lines) in the simulation models. The L-mode EMIC waves initially grow faster than the mirror mode waves.

[16] In Figure 3a, the effect of the mirror mode waves on the saturation levels of the L-mode EMIC waves is also shown. The initial linear growth rates of the L-mode EMIC

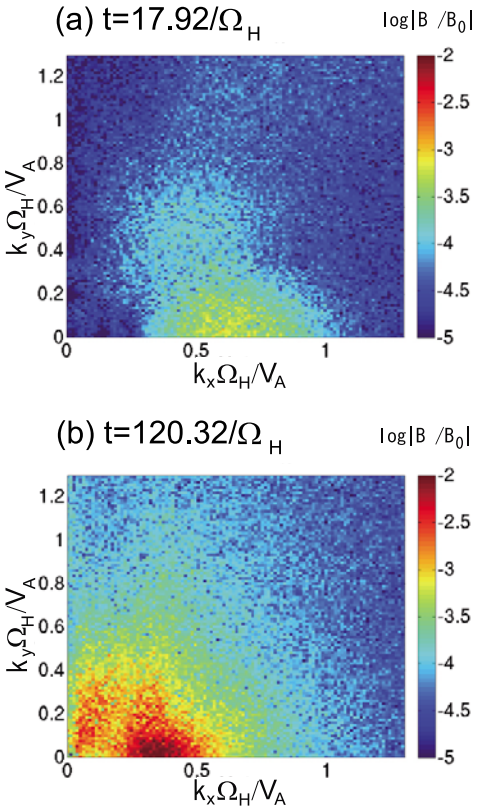

Figure 4. The spectrum of B/B_0 in the log scale in the two-dimensional model. (a) $t = 17.92/\Omega_H$ in the linear stage. (b) $t = 120.32/\Omega_H$ in the nonlinear stage.

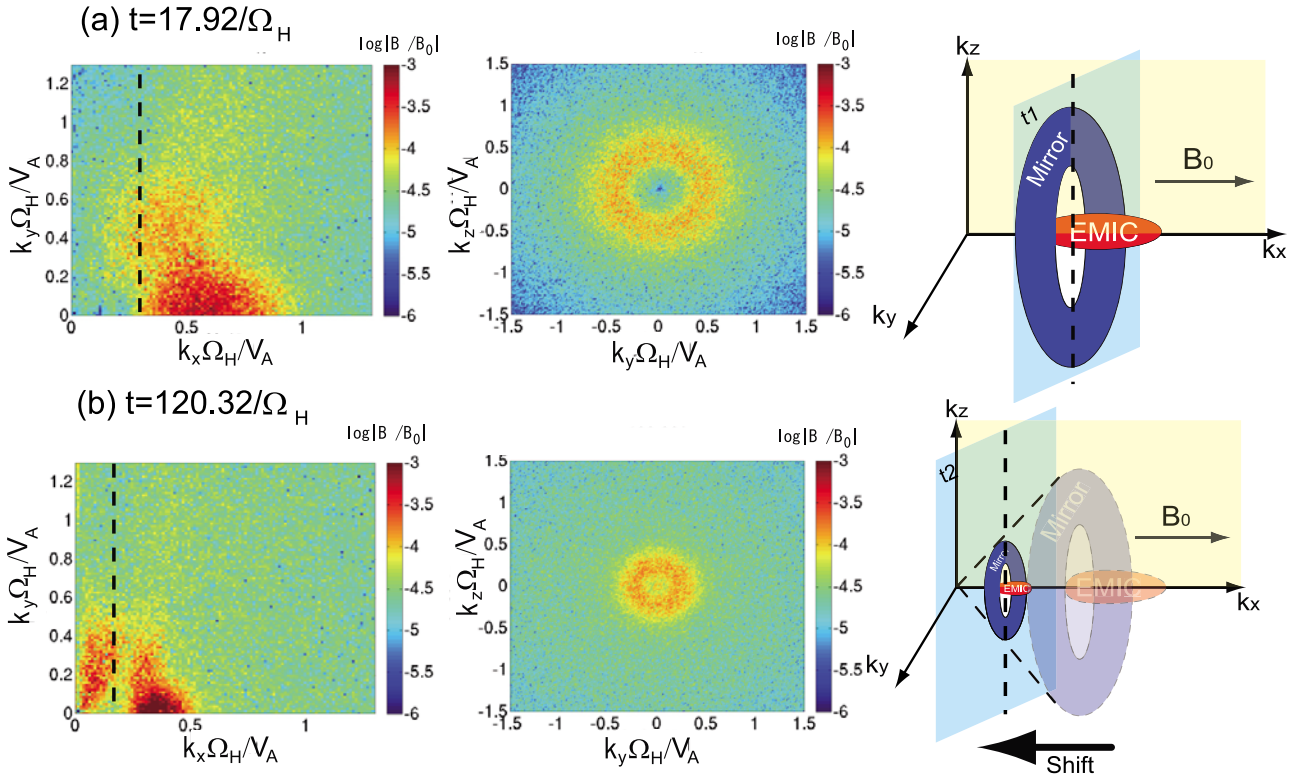

Figure 5. The log scale spectrum of B/B_0 in the three-dimensional model. A schematic drawing is shown for illustration. (a) $t = 17.92/\Omega_H$ in the linear stage. (b) $t = 120.32/\Omega_H$ in the nonlinear stage.

waves are the same in all simulation models. As we discuss later in section 3.6, the growth of the mirror mode waves relaxes the temperature anisotropy of protons more effectively in the three-dimensional model than in the two-dimensional model. As the spatial dimension increases, the available free energy for the L-mode EMIC instability are lost faster to the mirror mode waves, and the growth time of the L-mode waves becomes shorter. Therefore the saturation levels of the L-mode EMIC waves are very different in these two simulation models. Indeed, in the three-dimensional model, the mirror mode and L-mode EMIC waves have similar amplitudes for these parameters, whereas in one-dimensional or two-dimensional models, the L-mode EMIC waves dominate the mirror mode by over one order of magnitude in amplitude.

[17] The spectrum of $\boldsymbol{B}/B_0$ in the log scale in the two-dimensional and three-dimensional models at $t = t_1 = 17.92/\Omega_H$ are shown in Figures 4a and 5a, respectively. In Figure 5, the left and middle panels are the spectrum for $m_z = 1$ and $m_x = 26$ (which correspond to $k_z = 0V_A/\Omega_H$ and $k_x = 0.30V_A/\Omega_H$) planes, respectively. The right panel is a schematic drawing of the spectrum in the three-dimensional wave number space. In the wave number vector space of both models, note the mirror mode waves excited at oblique angles and the L-mode EMIC waves excited mostly in the direction parallel to $\boldsymbol{B}_0$. In Figure 4a and the left panel of Figure 5a, the L-mode EMIC waves are excited faster than the mirror mode waves. The spectrum of L-mode EMIC waves is much stronger than that of mirror mode waves, especially in two-dimensional model. This is because the growth rate of the L-mode EMIC wave is higher than that of the mirror mode wave. The mirror mode waves, on the other hand, grow slowly in oblique directions in both models. Because of symmetry, the spectrum of the mirror mode waves spreads in all perpendicular direction as shown in the middle panel of Figure 5a. All of the cross sections of the wave number space including x axis are the same. Therefore the mirror mode waves in the wave number space form a torus-like structure shown in the right panel of Figure 5a. In this panel, the center structure is the L-mode EMIC waves and the surrounding structures are the mirror mode waves.

[18] We identify the magnetic energy density of each wave by the following method and plot its time history in Figure 6. Examination of the wave spectra shows that the L-mode EMIC waves and mirror mode waves are separated by the angle $\theta = 30^\circ$ between the wave number vector $\boldsymbol{k}$ and $\boldsymbol{B}_0$. Accordingly, we define the "L-mode EMIC wave range" to be $0^\circ \leq \theta \leq 30^\circ$, and the "mirror mode wave range" to be $30^\circ < \theta \leq 80^\circ$. We divide the spectra of the magnetic field into these two ranges of the wave number vector space, and integrate the value of $|\boldsymbol{B}(\boldsymbol{k})/B_0|^2$ in each range. Figures 6a and 6b show results of the two-dimensional and three-dimensional simulations, respectively.

[19] We find a clear difference in the saturation levels of the L-mode EMIC and mirror instabilities in the two-dimensional and three-dimensional models. In the two-dimensional model, shown in Figure 6a, the magnetic energy density of the L-mode EMIC waves attains a larger value than that of the mirror mode waves. This is caused by the L-mode linear growth rate being larger than that of the mirror mode waves. In the three-dimensional model shown in Figure 6b, however, the mirror mode waves gains larger

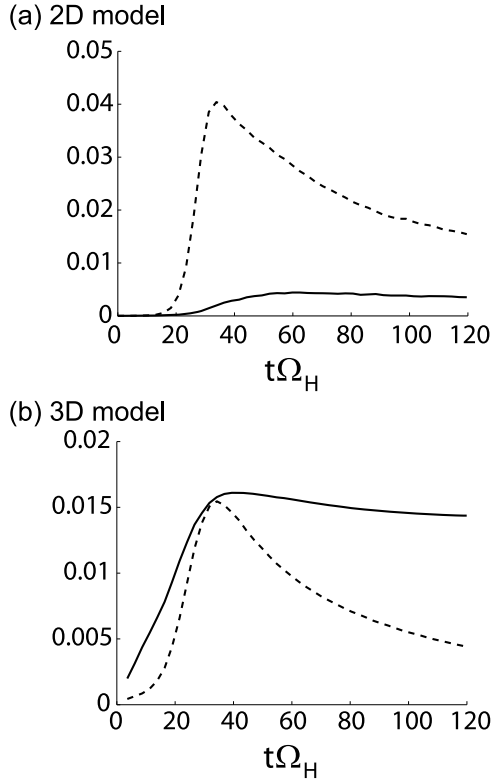

Figure 6. Time evolution of the magnetic energy density of the L-mode EMIC waves and the mirror mode waves in the (a) two-dimensional and (b) three-dimensional model. The dashed line shows the energy of the L-mode EMIC waves, and the solid line shows that of the mirror mode waves.

free energy than the L-mode EMIC wave. In the oblique direction region the mirror mode waves can exist over a wider range of the wave numbers because the degree of freedom of the wave number vector space increases because of another perpendicular direction k_z. In the two-dimensional model, the structures are uniform in the k_z direction, while in the three-dimensional model the wave number vectors of the mirror mode waves form the torus-like structure shown in the right panel of Figure 5a. As a result, the mirror mode waves gain more free energy than L-mode EMIC wave, even though the linear growth rate is still smaller than that for the L-mode EMIC wave.

3.3. Effect of Initial Thermal Fluctuation

[20] There is a possibility that the L-mode EMIC instability becomes dominant although the mirror instability obtains the geometrical three-dimensional advantage, as we have explained in the previous section. In much lower initial thermal noise case, the growth time of the L-mode EMIC waves becomes longer. As a result, the amplitude of the L-mode EMIC waves becomes larger than that in the higher noise case. In such extreme cases, the mirror instability will not dominate over the L-mode EMIC instability. We will calculate each wave energy density and estimate the effect of initial thermal fluctuation on the competition below.

[21] Since the timescale of the mirror instability is much slower than the cyclotron motion of protons, this phenomenon is gyrotropic and the spectrum in the wave number space becomes symmetric in the perpendicular plane. This is verified by the simulation result shown in Figure 5a. We assume a mirror mode wave which has only specified wave numbers $(k_\parallel, k_\perp) = (k_{\parallel M}, k_{\perp M})$; this forms a "ring" in the three-dimensional wave number space. The parallel component of the mirror mode wave is given by

$$B_{M\parallel}(k,t) = B_{M0}\delta\left(k_\parallel - k_{\parallel M}\right)\delta(k_\perp - k_{\perp M})e^{\gamma_M t}, \tag{8}$$

where B_{M0} is the initial thermal noise for the mirror mode wave, $k_\perp$ $(= \sqrt{k_y^2 + k_z^2})$ is the wave number in the perpendicular direction and $\delta(x)$ is Dirac's delta function.

[22] By inverse Fourier transform, we obtain the wave amplitude in the real space:

$$B_{M\parallel}(x,t) = \frac{k_{\perp M}B_{M0}}{(2\pi)^2}J_0\left(k_{\perp M}\sqrt{y^2+z^2}\right)e^{ik_{\parallel M}x+\gamma_M t}, \tag{9}$$

where $J_0(x)$ is the Bessel function of order 0. From $\nabla \cdot \boldsymbol{B} = 0$, we obtain the perpendicular component of the mirror mode wave, $B_{M\perp}$:

$$B_{M\perp} = -\frac{k_{\parallel M}}{k_{\perp M}}B_{M\parallel}. \tag{10}$$

We also obtain one of the transverse components of the L-mode EMIC wave at $(k_\parallel, k_\perp) = (k_{\parallel L}, 0)$ in the same manner:

$$B_{L\perp}(x,t) = \frac{B_{L0}}{(2\pi)^3}e^{i\left(k_{\parallel L}x-\omega_L t\right)+\gamma_L t}, \tag{11}$$

where B_{L0} is the initial thermal noise for the L-mode EMIC wave.

[23] We calculate variation of wave energy densities over the time period τ_g during which both wave modes grow according to the linear growth rates. Since the total amplitude of the mirror mode wave B_M can be expressed by $B_{M\parallel}$ as $B_M^2 = B_{M\perp}^2 + B_{M\parallel}^2 = (1 + k_{\parallel M}^2/k_{\perp M}^2)B_{M\parallel}^2$, we obtain the wave energy variation of the mirror mode wave:

$$\begin{aligned}\Delta\mathcal{E}_M &= \left\langle |B_M(x,\tau_g)|^2 - |B_M(x,0)|^2 \right\rangle \\ &= \frac{B_{M0}^2}{16\pi^3}\left(e^{2\gamma_M\tau_g}-1\right)\left(1+\frac{k_{\parallel M}^2}{k_{\perp M}^2}\right)\int_0^{2\pi}J_0^2(p)pdp,\end{aligned} \tag{12}$$

where $\langle x \rangle$ shows the mean value of x in the volume. On the other hand, the L-mode EMIC wave has two perpendicular components since it has the left-handed circular polarization. Thus, the total amplitude of the L-mode EMIC wave B_L can be expressed by $B_{L\perp}$ as $B_L^2 = B_{Ly}^2 + B_{Lz}^2 = 2B_{L\perp}^2$. From equation (11), we calculate the wave energy of the L-mode EMIC wave:

$$\Delta\mathcal{E}_L = \left\langle |B_L(x,\tau_g)|^2 - |B_L(x,0)|^2 \right\rangle = \frac{B_{L0}^2}{(2\pi)^6}\left(e^{2\gamma_L\tau_g}-1\right). \tag{13}$$

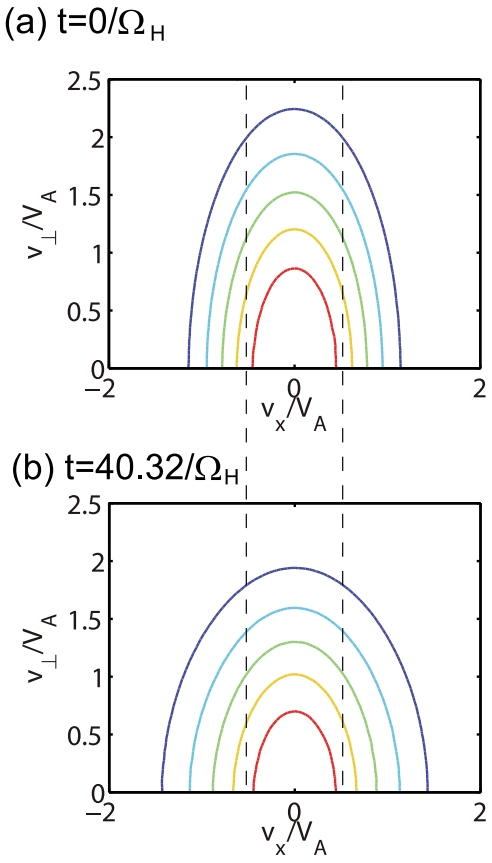

Figure 7. The isodensity curves of protons in the three-dimensional model (a) at $t = 0$ and (b) at $t = 40.32/\Omega_H$. The dashed lines show the resonance velocity of protons for the fastest growing mode of EMIC waves.

In the present simulation, at the end of the linear growing stage, we find that the energy of the mirror mode waves is larger than that of the L-mode EMIC waves. This is expressed as $\Delta\mathcal{E}_M/\Delta\mathcal{E}_L > 1$. Substituting equations (12) and (13) into the inequality, we obtain the condition of the initial thermal fluctuations for the dominance of the mirror instability:

$$\left(\frac{B_{L0}}{B_{M0}}\right)^2 < 4\pi^3 \frac{e^{2\gamma_M\tau_g}-1}{e^{2\gamma_L\tau_g}-1}\left(1+\frac{k_{\parallel M}^2}{k_{\perp M}^2}\right)\int_0^{2\pi} J_0^2(p)pdp \simeq 23.2\frac{e^{2\gamma_M\tau_g}-1}{e^{2\gamma_L\tau_g}-1}\left(1+\frac{k_{\parallel M}^2}{k_{\perp M}^2}\right). \quad (14)$$

Assuming $B_{M0} = B_{L0}$ and $e^{2\gamma t} \gg 1$, the value of τ_g should satisfy the condition (15):

$$\tau_g < \frac{\log\left(1+k_{\parallel M}^2/k_{\perp M}^2\right)+3.14}{2(\gamma_L-\gamma_M)}. \quad (15)$$

Substituting the simulation parameters, $\gamma_M = 0.16\Omega_H$, $\gamma_L = 0.28\Omega_H$, $k_{\perp M}/k_{\parallel M} = \tan 50°$, into equation (15), we obtain the condition for the dominance of the mirror instability:

$$\tau_g < 16.8/\Omega_H. \quad (16)$$

From Figure 3, we confirm that the value of τ_g in the simulation satisfies this condition. Assuming $\tau_g\Omega_H \gg 1$, we rewrite equation (14) as

$$\frac{B_{L0}}{B_{M0}} < 7.49e^{-(\gamma_L-\gamma_M)\tau_g}. \quad (17)$$

If the initial fluctuations can satisfy this condition, the mirror mode wave can gain more free energy than the L-mode EMIC wave, even though γ_L is larger than γ_M. In an extreme case where B_{L0} is much larger than B_{M0}, the L-mode EMIC instability will dominate over the mirror instability. However, the realistic conditions $B_{M0} \sim B_{L0}$ and $(\gamma_L - \gamma_M)\tau_g < 2$ result in the dominance of the mirror mode wave.

3.4. Long Time Evolution of L-Mode EMIC Wave

[24] The mirror mode instability in the three-dimensional model effectively diffuse the temperature anisotropy as we discuss in section 3.6. It makes the linear growth rates and wave numbers of L-mode EMIC waves smaller than those in the two-dimensional model before the end of the growth phase. The L-mode EMIC waves still grow as we can see in Figure 3a (around $20/\Omega_H < t < 30/\Omega_H$). When the amplitude of the L-mode EMIC waves reaches a sufficient level, the forward and backward propagating waves form a nonlinear static potential Φ which is produced by the $\boldsymbol{v}_\perp \times \boldsymbol{B}_\perp$ term [*Omura et al.*, 1988; *Omura*, 1991]. It can be expressed as

$$\Phi = \frac{m}{q}\left(\frac{\Omega_H}{k}\frac{B_{L\perp}}{B_0}\right)^2 \frac{\omega}{\Omega_H-\omega}\cos(2kx+\theta_0), \quad (18)$$

where, θ_0 is the phase at $x = 0$. Because of particle trapping by this nonlinear potential, the energy of the L-mode EMIC waves is transferred to proton kinetic energy. Figure 7 shows the isodensity curves of the protons at the initial time and at the saturation time. We find heating of the whole proton distribution function caused by the nonlinear trapping.

[25] We also note that there is another nonlinear effect of the L-mode EMIC waves. As we can see in Figure 4b and the left panel of Figure 5b, which show the spectra at $t = t_2 = 120.32/\Omega_H$, the spectrum of the L-mode EMIC waves in the two-dimensional and three-dimensional models shifts to lower wave numbers. This transfer of the energy from higher wave numbers to lower wave numbers is due to a nonlinear effect. To show details of the nonlinear evolution of the L-mode EMIC waves, we focused on the spectra of the electric and magnetic fields at $k_y = k_z = 0$. Figure 8 shows $\log|B_\perp(k_x, t)/B_0|$ and $\log|E_\parallel/(V_A B_0)|$ in the one-dimensional, two-dimensional and three-dimensional models. The $B_\perp(k_x, t)$ component and $E_\parallel(k_x, t)$ component include only the L-mode EMIC wave and acoustic wave, respectively. At the initial stage, the L-mode EMIC waves are excited and there is no $E_\parallel(k_x, t)$ component because the L-mode EMIC wave is a purely transverse wave. After linear growth, the spectrum of the dominant L-mode EMIC waves starts to shift to lower wave number vectors, and the acoustic wave is generated at higher wave numbers than the $B_\perp(k_x, t)$ component, and it also shifts to the lower wave numbers. Although the growth rate of the EMIC instability decreases, the EMIC waves still grow to a sufficient amplitude that induces the parallel heating of resonant protons by the nonlinear potentials and the

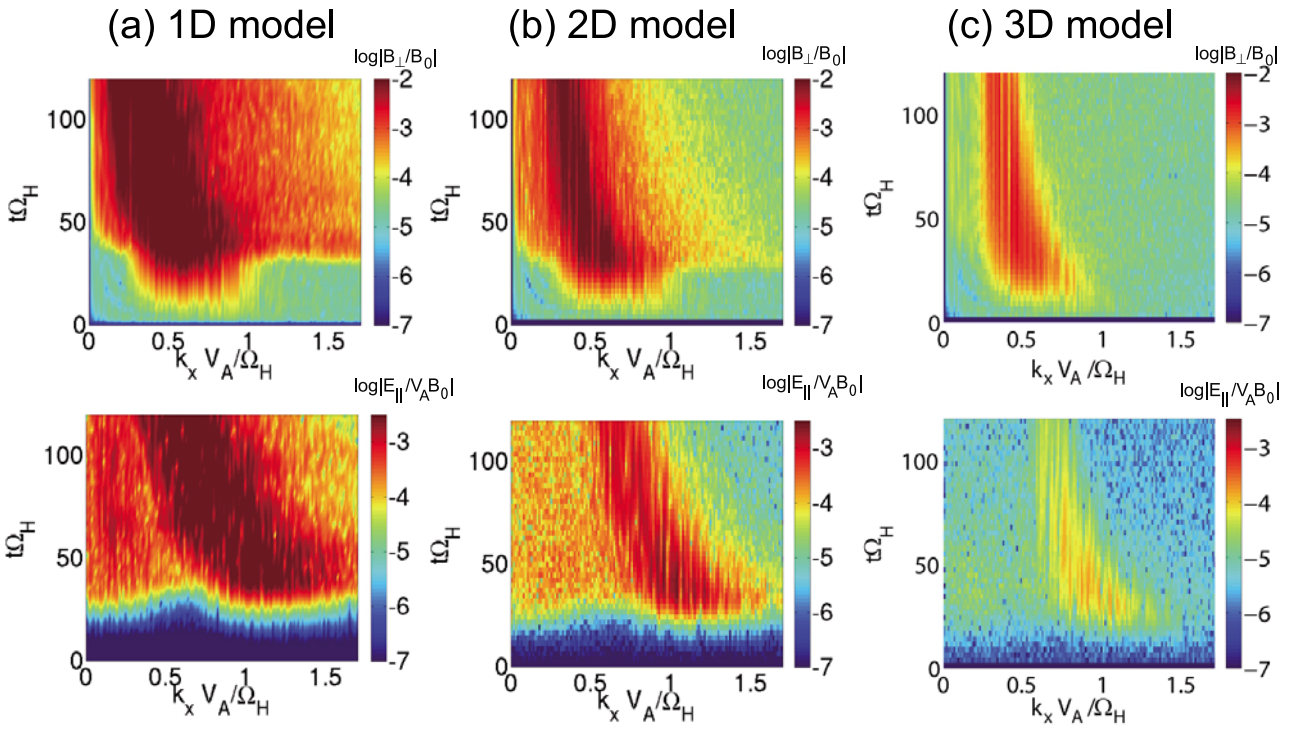

Figure 8. The spectra of $\boldsymbol{B}_{\perp}(k_x, t)/B_0$ (EMIC wave) and $\boldsymbol{E}_{\parallel}(k_x, t)/(B_0 V_A)$ (acoustic wave) in the log scale in the (a) one-dimensional, (b) two-dimensional, and (c) three-dimensional models.

inverse cascading process. These nonlinear processes terminate the growth of the EMIC waves.

[26] Figures 9a and 9b show the dispersion relations (ω-k_x diagram) of the L-mode EMIC waves during $0 < t < 25.6/\Omega_H$ and the ion acoustic waves during $25.6/\Omega_H < t < 51.2/\Omega_H$, respectively. The white curve in Figure 9a is the dispersion relation that we obtained by linear analysis (see section 2). Because we use a Fourier transform for a short time interval, the spectrum obtained by the simulation is broad in frequency. There are forward and backward propagating L-mode EMIC waves present. We choose one each of the forward and backward propagating waves, and show them by red arrows. These two waves and the parallel propagating ion acoustic waves (which are shown by the yellow arrow), satisfy momentum and energy conservation relations (19) and (20) shown in the works of *Sagdeev and Galeev* [1969] and *Terasawa et al.* [1986].

$$k_f = -k_b + k_{ia} \tag{19}$$

$$\omega_f = \omega_b + \omega_{ia} \tag{20}$$

In the above (k_f, ω_f) and (k_b, ω_b) are sets of the wave number and the frequency for the forward and backward propagating L-mode EMIC wave, respectively, and (k_{ia}, ω_{ia}) is the same for the ion acoustic wave. These three points and the origin (0, 0) form a parallelogram in the ω-k_x diagram. In this three-wave coupling process, the energy of the forward propagating mode is converted to the backward propagating mode and the ion acoustic mode. Because of the symmetry of the simulation space, the same nonlinear process takes place in the opposite direction. This means that we have another parallelogram with the backward propagating mode. The phase velocity of the ion acoustic wave is given as

$$\frac{\omega_{ia}}{k_{ia}} = \frac{\omega_f - \omega_b}{k_f + k_b} \simeq 0.1 \ll V_{\parallel H}, \tag{21}$$

and thus the energy of the ion acoustic mode is effectively used to heat the protons. The L-mode EMIC waves lose their energy and their spectra cascade to lower wave numbers. Figure 9c shows the dispersion relation computed in the range of $25.6/\Omega_H < t < 51.2/\Omega_H$. The red arrows in this panel indicates the forward and the generated backward propagating waves.

[27] Figure 10 shows further evidence for the nonlinear effect on the L-mode EMIC waves. Red lines and blue lines show the amplitude of the L-mode EMIC waves at the higher and lower wave number, respectively. Initially, the higher modes grow linearly in each model. In the two-dimensional model, after the higher modes stop growing, they start to decrease and the lower modes start to grow. Therefore shift of the spectrum of L-mode EMIC waves are mainly caused by the nonlinear effect in the two-dimensional model. On the other hand, in the three-dimensional model, one of the lower modes (m_x = 21) initially grows slowly at the initial time and another one starts to grow after the higher modes saturate. This means the linear effect and the nonlinear effect coexist in the three-dimensional model. The shift of the spectrum is caused by these factors. The magnetic field energy of L-mode EMIC waves takes the maximum value and subsequently decreases to a constant level in both two-dimensional and three-dimensional models.

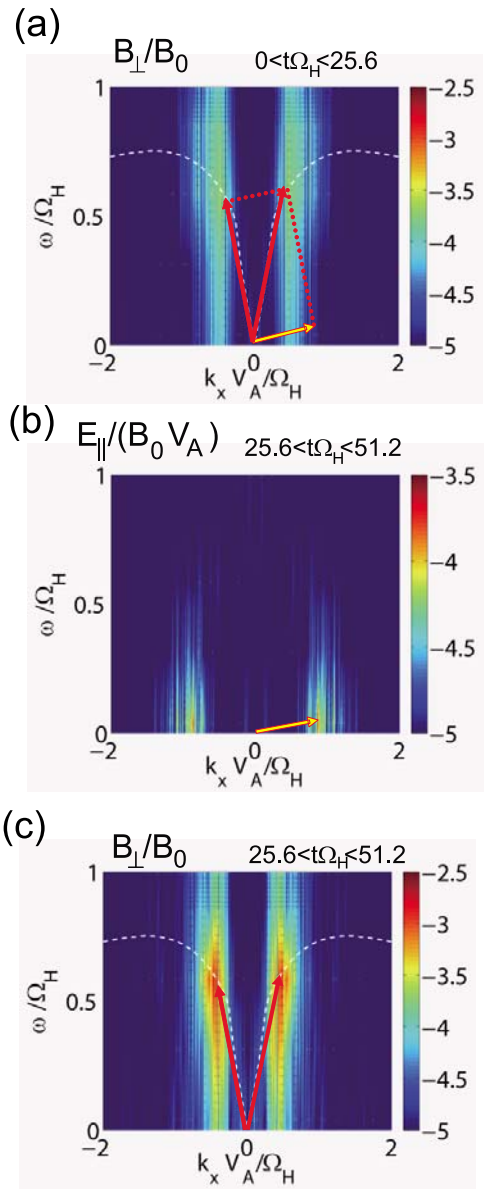

Figure 9. The dispersion relation (ω-$k_{||}$ diagram) of the L-mode EMIC waves at (a) $0 < t\Omega_H < 25.6$ and (c) $25.6 < t\Omega_H < 51.2$ and that of the ion acoustic waves at (b) $25.6 < t\Omega_H < 51.2$. The red arrows show forward and backward propagating L-mode EMIC waves, respectively. The yellow arrows indicate a forward propagating ion acoustic wave.

3.5. Long Time Evolution of Mirror Mode Structure

[28] Since protons are heated in the parallel direction by the nonlinear evolution of the L-mode EMIC waves, the temperature anisotropy reaches the threshold of the mirror instability, and thus the mirror mode waves stop growing. In Figure 4b and the left panel of Figure 5b, we can find that the wave numbers of the excited mirror mode waves also change in wave number space in both models. The energy of the magnetic field that exists in the large wave number modes is transferred to smaller wave number modes. In the three-dimensional model, this means the torus-like structure in the wave number space changes its form to the smaller one in the lower wavenunber as shown in the right panel of Figure 5b.

[29] In Figure 11, which shows the time evolution of $B_{||}$ at $t\Omega_H$ = 17.92, 30.72, 43.52, and 120.32, we find clear formation of magnetic structures of the mirror mode waves in both two-dimensional and three-dimensional models. In these panels, the color bar is tuned to show the clear structures. The actual maximum values of the amplitude are 0.31 and 0.63 in the two-dimensional and three-dimensional models, respectively. It is noted that the L-mode EMIC waves do not have any parallel component of the magnetic field. Since there are no k_z component of the wave number vector in the two-dimensional model, stripes of magnetic structures are formed. In the three-dimensional model, the mirror mode structures are different from those in the two-dimensional model because of the third dimension. In both two-dimensional and three-dimensional models, the mirror mode waves remain as larger structures at the end of the simulations ($t = t_2$).

[30] As we can see in Figure 6b, the energy of the mirror mode waves does not decrease as much as in the case of the L-mode EMIC waves. This means coalescence of the mirror mode waves does not contribute to the heating of protons in the nonlinear stage. Then, the nonlinear evolution is dominated by the inverse cascading of the L-mode EMIC waves. This is another reason why the mirror instability is dominant in the magnetosheath.

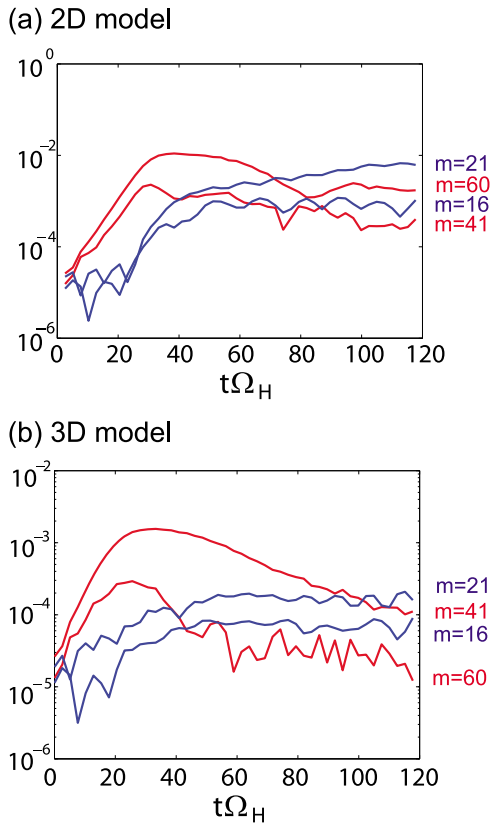

Figure 10. The amplitude of the L-mode EMIC wave for the various mode numbers (m = 60, 41 with red line and m = 21, 16 with blue line) in the (a) two-dimensional and (b) three-dimensional models.

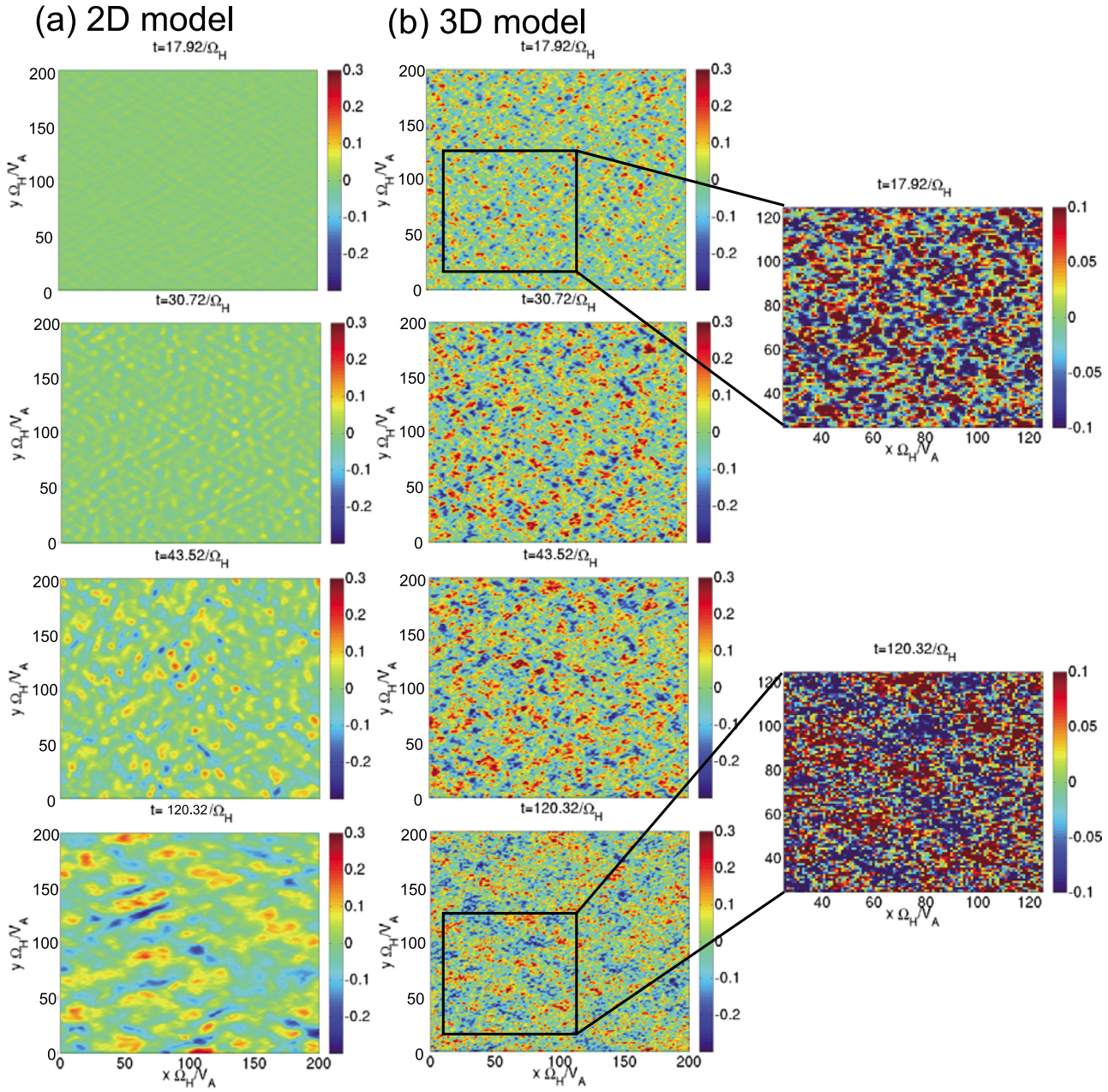

Figure 11. The time evolution of $\boldsymbol{B}_{\parallel}/B_0$ in the x-y plane in the (a) two-dimensional and (b) three-dimensional models.

3.6. Heating of Particles

[31] Figure 12a shows the difference of the relaxation of the temperature anisotropy in the three different simulation models. Since there is no mirror mode wave in the one-dimensional model, the L-mode EMIC instability consumes all of the free energy of the temperature anisotropy. In the two-dimensional model, the L-mode EMIC waves are affected by the mirror instability, but the amplitude at the linear growth stage still becomes much larger than that of the mirror instability. In the linear stage, because of the dominance of the mirror instability, the temperature anisotropy in the three-dimensional model decreases more quickly than that in the one-dimensional and two-dimensional models. The spreading of the energy spectrum of the mirror mode waves in the three-dimensional model causes the effective consumption of the free energy of the temperature anisotropy.

[32] After the energy density of each wave saturates, the anisotropy of protons is relaxed slower than that before saturation. Because of the heating by the nonlinear potential and the inverse cascading process, the L-mode EMIC waves lose their energy to thermalize the background protons, and therefore the system is dominated by the mirror mode waves in the nonlinear stage. In the later time, the temperature anisotropy in each model is almost the same. The nonlinear evolution of the L-mode EMIC instability is almost in the parallel direction in each model, the protons are heated by the nonlinear potential and the parallel propagating ion acoustic waves at the nonlinear stage. This heating is less

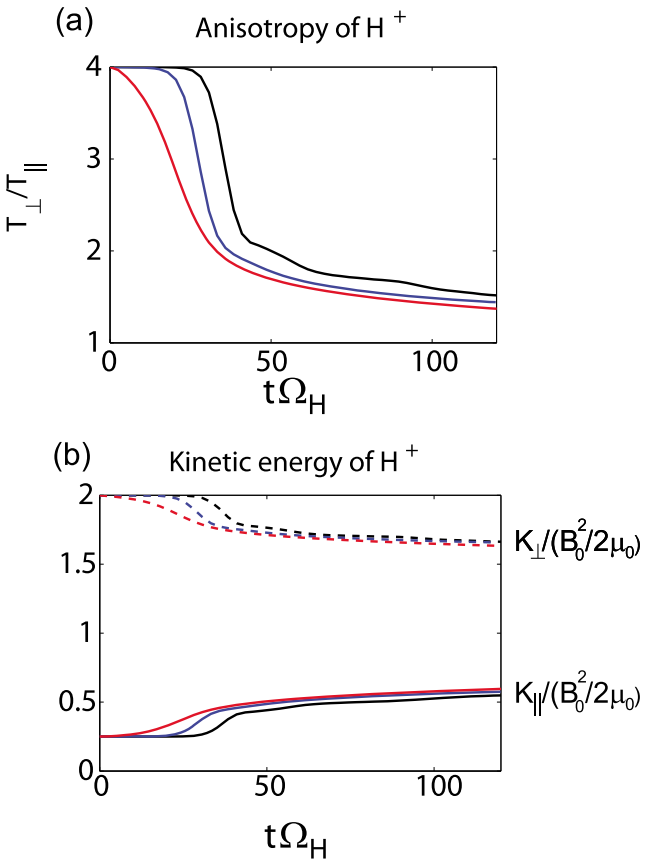

Figure 12. (a) The relaxation of the temperature anisotropy of protons. The black line shows the result in the one-dimensional model, the blue line shows that in the two-dimensional model, and the red line shows that in the three-dimensional model. (b) The kinetic energy of H^+ in each direction. The solid line shows the kinetic energy in the parallel direction, and the dashed line shows that in the perpendicular direction in each model.

dependent on the differences of the spatial dimension. Then, the particles should be heated to almost the same level among the three models. Figure 12b shows the kinetic energy density of protons in each model. We can find that the kinetic energies in the parallel and perpendicular directions are almost the same among the three models.

[33] Figure 13 shows the time evolution of the energy in the three-dimensional model up to $t = t_2 = 120.32/\Omega_H$. Figure 13a shows the magnetic energy density of each wave. The solid black line shows $|\boldsymbol{B}/B_0|^2$ of the mirror mode waves, and the dashed black line shows $|\boldsymbol{B}/B_0|^2$ of the L-mode EMIC waves. In the nonlinear stage, the energy of the L-mode EMIC waves decreases and the kinetic energy of protons in the parallel direction increases. As the simulation space is the uniform model with the periodic boundary, the initially given total energy should be conserved. Then, the magnetic energy which decreases at the nonlinear stage should go into kinetic energy of protons.

[34] Figure 13b shows the value of $\boldsymbol{J_i} \cdot \boldsymbol{E}/(B_0^2\Omega_H/\mu_0)$, where $\boldsymbol{J_i}$ is the ion current. Note that when $\boldsymbol{J_i} \cdot \boldsymbol{E} > 0$, the energy of electromagnetic waves goes to particles and vice versa. The timescale of the interaction between the ion acoustic waves and protons is much faster than that of the change of the mirror mode structure. The effect of the induced electric field due to the slow time variation of the magnetic field is much smaller than that of the ion acoustic waves. Thus the energy of the mirror mode waves does not go to protons. Figure 13c shows that the energy of the L-mode EMIC waves goes to protons through $\boldsymbol{J_i} \cdot \boldsymbol{E}$.

[35] From the energy conservation law, we can obtain,

$$\frac{\partial^2 u_m}{\partial t^2} = -\frac{\partial \boldsymbol{J}_i \cdot \boldsymbol{E}}{\partial t}, \tag{22}$$

where u_m is the average of the magnetic energy density in the simulation space. In the hybrid simulation, if we assume the phase speed is much slower than the speed of light c, then the electric energy density $u_e = E^2/2c^2$ term can be neglected. Because the net system energy is conserved such as $u_m + K_H = const.$, the second derivative of the kinetic energy $\partial^2 K_H/\partial t^2$ is equal to $-\partial^2 u_m/\partial t^2$. In the growing

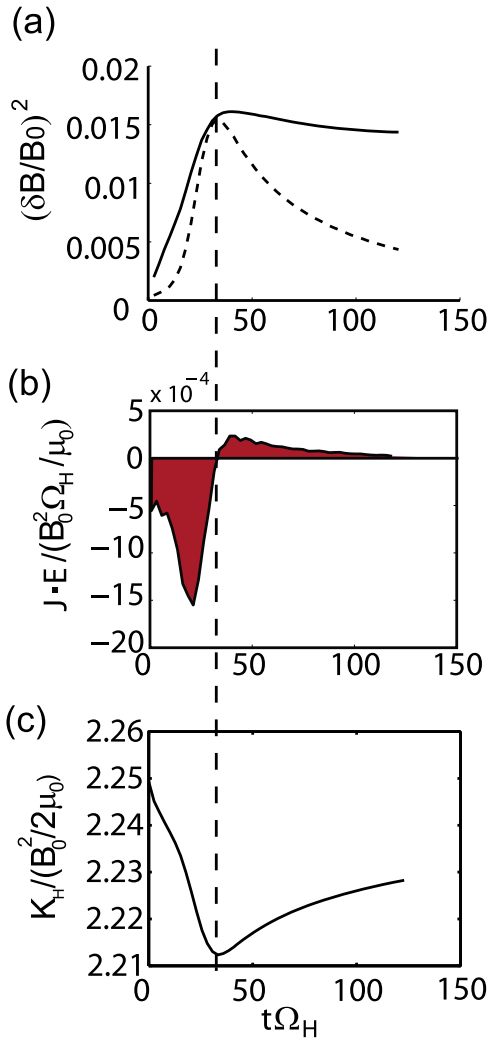

Figure 13. The time evolution of kinetic and magnetic energy in the three-dimensional model. (a) The magnetic energy density of each mode. (b) The integrated value of $\boldsymbol{J} \cdot \boldsymbol{E}/(B_0^2\Omega_H/\mu_0)$ in the simulation space. (c) The kinetic energy density of protons $K_H/(B_0^2/2\mu_0)$ in the three-dimensional model.

phase, when the sign of $\partial^2 u_m/\partial t^2$ is positive, the electromagnetic waves grow exponentially, and when it is negative, they suffer from the nonlinear effect. Then, equation (22) indicates we can judge whether linear or nonlinear growth is dominant in the growing phase with the sign of the derivative of $\boldsymbol{J_i} \cdot \boldsymbol{E}/(B_0^2\Omega_H/\mu_0)$. At the minimal point of $\boldsymbol{J_i} \cdot \boldsymbol{E}/(B_0^2\Omega_H/\mu_0)$, there is the point of change from linear growth to nonlinear growth. From Figure 13b, showing $\boldsymbol{J_i} \cdot \boldsymbol{E}/(B_0^2\Omega_H/\mu_0)$, we find the time at the minimal point is $t = 23.04/\Omega_H$, and this time agrees with the time when the ion acoustic waves are generated (from the bottom panel of Figure 8c).

4. Discussion and Conclusions

[36] By expanding the simulation system from a two-dimensional model to a three-dimensional model, we find that the mirror instability dominates over the L-mode EMIC instability because the mirror mode waves form torus-like structures in the three-dimensional wave number space as shown in Figure 5a. We also derived the theoretical condition of the initial thermal fluctuations for the dominance of the mirror instability. The realistic conditions result in the dominance of the mirror mode wave.

[37] The saturation level of the L-mode EMIC waves in the three-dimensional model becomes smaller than those in the one-dimensional and two-dimensional models because the mirror instability effectively consumes the free energy of the temperature anisotropy. In Figure 7, we found the nonlinear heating of the whole proton distribution functions. We cannot find the quasilinear effect which occurs near the resonance velocity of the fastest growing mode of EMIC waves ($\simeq 0.4V_A$). We therefore conclude that saturation of the L-mode EMIC waves is caused by heating by the nonlinear potentials and by nonlinear wave-wave coupling.

[38] In the nonlinear stage, the kinetic energy is almost the same among the one-dimensional, two-dimensional, and three-dimensional models as shown in Figure 12a. From Figure 6, we find the nonlinear evolution is dominated by the L-mode EMIC instability. In all models, the L-mode EMIC waves transfer their energy to ion heating by the nonlinear potentials and the generated ion acoustic waves. With these nonlinear processes, the L-mode EMIC waves lose their energy quickly. These phenomena take place with the parallel propagating waves, and thus the nonlinear heating occurs almost in the parallel direction. Because of these nonlinear heating of protons in the parallel direction, the temperature anisotropy decreases to the threshold of the mirror instability, and thus the growth of the mirror mode waves saturates.

[39] Coalescence of the mirror mode structures proceeds after the saturation of the mirror instability in both two-dimensional and three-dimensional models. The topology of the mirror mode structures in the three-dimensional model differs from that in the two-dimensional model because of the difference in degree of freedom in the perpendicular direction. This causes a clear difference in nonlinear evolution of the magnetic field structures. At the end of the nonlinear evolution, these structures still remain. This coalescence occurs on a longer timescale than for inverse cascading of the L-mode EMIC waves. In the magnetosheath, this nonlinear effect on the dominance of mirror instability should occur not near the bow shock but in regions of the deep magnetosheath or magnetopause, where the L-mode EMIC waves have reached nonlinear levels and are decaying. Therefore, it is likelier to observe mirror mode waves in inside the magnetosheath rather than near the bow shock.

[40] We note that *Tsurutani et al.* [1982] has measured the scale size of mirror mode waves at Earth and found it to be much larger than the ion inertial length. As the ion beta and temperature anisotropy becomes lower, the wavelength of the most unstable mode becomes larger [*Hasegawa*, 1969]. This mode, however, cannot grow enough because the maximum growth rate is small, and the temperature anisotropy is mostly consumed by the L-mode EMIC wave. We found that the scale size becomes larger and comparable to the observed one through the coalescence process as shown in Figure 11. The wave amplitude is still large after this nonlinear process takes place, and the observed mirror mode waves also have large amplitude. Therefore, the large mirror mode structure in the magnetosheath should be caused by not only the linear growth but also the nonlinear process. For more precise comparison with the observations, more parametric analyses are needed, and moreover the nonlinear evolution must be followed in an open system with anisotropic ion population injected upstream of the magnetosheath. Such simulations are left as a future study.

[41] To our knowledge, this is the first study to analyze the competing process between the L-mode EMIC instability and the mirror instability by the three-dimensional hybrid simulation. Mirror instability becomes dominant for two reasons: the large volume of the mirror mode waves in the three-dimensional wave number space and the quick dissipation of the L-mode EMIC waves due to nonlinear evolution. More analysis for the slower nonlinear process is left for the future work.

Appendix A: Derivation of the Waveform of the Mirror Mode Wave in the Three-Dimensional Model

[42] Calculating the Inverse Fourier Transform of equation (8), we obtain the waveform in the real space:

$$\begin{aligned} B_{M\parallel}(x,t) &= \frac{B_{M0}}{(2\pi)^3}\int \delta(k_\parallel - k_{\parallel M})e^{ik_\parallel x}dk_\parallel \\ &\quad\cdot \iint \delta(k_\perp - k_{\perp M})e^{i(yk_y+zk_z)}dk_y dk_z e^{\gamma_M t} \\ &= \frac{B_{M0}}{(2\pi)^3}e^{ik_{\parallel M}x+\gamma_M t}\iint \delta(k_\perp - k_{\perp M})e^{i(yk_y+zk_z)}dk_y dk_z. \end{aligned} \tag{A1}$$

We change the orthogonal coordinates to the polar coordinates, $(k_y, k_z) \mapsto (k_\perp, \phi)$, and then equation (A1) is calculated as

$$\begin{aligned} B_{M\parallel}(x,t) &= \frac{B_{M0}}{(2\pi)^3}e^{ik_{\parallel M}x+\gamma_M t} \\ &\quad\cdot \iint \delta(k_\perp - k_{\perp M})e^{i(yk_\perp\cos\phi+zk_\perp\sin\phi)}k_\perp dk_\perp d\phi \\ &= \frac{k_{\perp M}B_{M0}}{(2\pi)^3}e^{ik_{\parallel M}x+\gamma_M t}\int_0^{2\pi} e^{ik_{\perp M}(y\cos\phi+z\sin\phi)}d\phi. \end{aligned} \tag{A2}$$

The phase part in the integrated function is calculated as $y\cos\phi + z\sin\phi = \sqrt{y^2+z^2}\cos(\phi+\phi_0)$, where $\phi_0 = \tan^{-1}(z/y)$ ($\tan^{-1}x$ is arctangent function). Therefore we obtain $B_{M\parallel}(\boldsymbol{x}, t)$ in the three-dimensional model as

$$B_{M\parallel}(x,t) = \frac{k_{\perp M}B_{M0}}{(2\pi)^3}e^{ik_{\perp M}x+\gamma_M t}\int_0^{2\pi} e^{ik_{\perp M}\sqrt{y^2+z^2}\cos(\phi+\phi_0)}d\phi = \frac{k_{\perp M}B_{M0}}{(2\pi)^2}J_0\left(k_{\perp M}\sqrt{y^2+z^2}\right)e^{\gamma_M t+ik_{\parallel M}x}, \quad \text{(A3)}$$

where $J_0(x)$ is the Bessel function of order 0. The value of ϕ_0 can be neglected because of the periodicity of the integrated function.

[43] **Acknowledgments.** Computation in the present study was performed with the KDK system of Research Institute for Sustainable Humanosphere (RISH) and Academic Center for Computing and Media Studies at Kyoto University as a collaborative research project. The present study was supported in part by a Grant-in-Aid for Research Fellows from the Japan Society for the Promotion of Science (JSPS). This work was partially supported by 17GS0208 for Creative Scientific Research "The Basic Study of Space Weather Prediction" of the Ministry of Education, Science, Sports and Culture of Japan. Portions of this work were performed at the Jet Propulsion Laboratory, California Institute of Technology, under contract with the National Aeronautics and Space Administration.

[44] Amitava Bhattacharjee thanks the reviewers for their assistance in evaluating this paper.

References

Bavassano, B., E. Pietropaolo, and R. Bruno (1998), Cross-helicity and residual energy in solar wind turbulence: Radial evolution and latitudinal dependence in the region from 1 to 5 AU, *J. Geophys. Res.*, *103*(A4), 6521–6529.

Birdsall, C. K., and A. B. Langdon (1985), Plasma physics via computer simulation, McGraw-Hill, New York.

Brinca, A. L., and B. T. Tsurutani (1989), Influence of multiple ion species on low-frequency electromagnetic wave instabilities, *J. Geophys. Res.*, *94*, 13,565.

Chandrasekhar, S. A., A. N. Kaufman, and K. M. Watson (1958), The stability of the pinch, *Proc. R. Soc. Lond. Ser. A*, *245*, 435.

Erdos, G., and A. Balogh (1996), Statistical properties of mirror mode structures observed by Ulysses in the magnetosheath of Jupiter, *J. Geophys. Res.*, *101*, 1.

Fuselier, S. A., B. J. Anderson, S. P. Gary, and R. E. Denton (1994), Inverse correlations between the ion temperature anisotropy and plasma beta in the Earth's quasi-parallel magnetosheath, *J. Geophys. Res.*, *99*, 14,931.

Gary, S. P. (1992), The mirror and ion cyclotron anisotropy instabilities, *J. Geophys. Res.*, *97*, 8519.

Gary, S. P., S. A. Fuselier, and B. J. Anderson (1993), Ion anisotropy instabilities in the magnetosheath, *J. Geophys. Res.*, *98*, 1481.

Glassmeier, K. H., P. N. Mager, and D. Y. Klimushkin (2003), Concerning ULF pulsations in Mercury's magnetosphere, *Geophys. Res. Lett.*, *30*(18), 1928, doi:10.1029/2003GL017175.

Hasegawa, A. (1969), Drift mirror instability in the magnetosphere, *Phys. Fluids*, *12*, 2642.

Hasegawa, A. (1975), Plasma instabilities and nonlinear effects, *Phys. Chem. Space*, *8*, 94, Springer-Verlag, New York.

Hubert, D. (1994), Nature and origin of wave modes in the dayside Earth magnetosheath, *Adv. Space Res.*, *14*(7), 55.

Kennel, C. F., and H. E. Petschek (1966), Limit of stably trapped particle fluxes, *J. Geophys. Res.*, *71*, 1.

Kennel, C. F., F. Coroniti, J. Arons, R. Blandford, and M. Israel (1985), Perspectives on space and astrophysical plasma physics, *Symp. - Int. Astron. Union*, 537.

Lacombe, C., and G. Belmont (1995), Waves in the Earth's magnetosheath: Observations and interpretations, *Adv. Space Res.*, *15*(8/9), 329.

Matsumoto, H., and Y. Omura (1993), *Computer Space Plasma Physics*, Terra Sci., Tokyo.

Midgeley, J. E., and L. Davis Jr. (1963), Calculation by a moment technique of the perturbation of the geomagnetic field by the solar wind, *J. Geophys. Res.*, *68*, 5111.

Omura, Y. (1991), Comment on "Particle Simulation of Ion Heating in the Ring Current" by S. Qian, M. K. Hudson, and I. Roth, *J. Geophys. Res.*, *96*, 7929.

Omura, Y., H. Usui, and H. Matsumoto (1988), Parallel heating associated with interaction of forward and backward electromagnetic cyclotron waves, *J. Geomag. Geoelectr.*, *40*, 949.

Phan, T. D., G. Paschmann, W. Baumjohann, N. Sckopke, and H. Luhr (1994), The magnetosheath region adjacent to the dayside magnetopause: AMPTE/IRM observations, *J. Geophys. Res.*, *99*, 121.

Price, C. P., D. W. Swift, and L. C. Lee (1986), Numerical simulation of nonoscillatory mirror waves at the Earth's magnetosheath, *J. Geophys. Res.*, *91*(A1), 101–112.

Russell, C. T., P. Song, and R. P. Lepping (1989), The Uranian magnetopause: Lessons from Earth, *Geophys. Res. Lett.*, *16*, 1485.

Sagdeev, R. Z., and A. A. Galeev (1969), *Nonlinear Plasma Theory*, p. 8, W. A. Benjamin, New York.

Terasawa, T., M. Hoshino, J.-I. Sakai, and T. Hada (1986), Decay instability of finite-amplitude circularly polarized Alfven waves: A numerical simulation of stimulated Brillouin scattering, *J. Geophys. Res.*, *91*, 4171.

Tsurutani, B. T., E. J. Smith, R. R. Anderson, K. W. Ogilvie, J. D. Scudder, D. N. Baker, and S. J. Bame (1982), Lion roars and nonoscillatory drift mirror waves in the magnetosheath, *J. Geophys. Res.*, *87*, 6060.

Tsurutani, B. T., I. G. Richaradson, R. P. Lepping, R. D. Zwickl, D. E. Jones, E. J. Smith, and S. J. Bame (1984), Drift mirror mode waves in the distant ($x \sim 200$ RE) magnetosheath, *J. Geophys. Res.*, *11*, 11,102.

Tsurutani, B. T., D. J. Southwood, E. J. Smith, and A. Balogh (1992), Nonlinear magnetosonic waves and mirror mode structures in the March 1991 Ulysses interplanetary event, *Geophys. Res. Lett.*, *19*, 1267.

Tsurutani, B. T., D. J. Southwood, E. J. Smith, and A. Balogh (1993), A survey of low-frequency (LF) waves at Jupiter: The Ulysses encounter, *J. Geophys. Res.*, *98*, 21,203.

Tsurutani, B. T., G. S. Lakhina, E. J. Smith, B. Buti, S. L. Moses, F. V. Coroniti, A. L. Brinca, J. A. Slavin, and R. D. Zwickl (1999), Mirror mode structures and ELF plasma waves in the Giacobini-Zinner magnetosheath, *Nonlinear Proc. Geophys.*, *6*, 229.

Violante, L., B. Cattaneo, G. Moreno, and J. D. Richardson (1995), Observations of mirror mode and plasma depletion layer upstream of Saturn's magnetopause, *J. Geophys. Res.*, *100*, 12,047.

Zwan, B. J., and R. A. Wolf (1976), Depletion of the solar wind plasma near a planetary boundary, *J. Geophys. Res.*, *81*, 1636.

B. Lembege, LATMOS-UVSQ-IPSL-CNRS, 10–12, Avenue de l'Europe, F-78140 Velizy, France.

Y. Omura and M. Shoji, Research Institute of Sustainable Humanosphere, Kyoto University, Gokasho, Uji, Kyoto 611-0011, Japan. (shouji@rish.kyoto-u.ac.jp)

B. T. Tsurutani and O. P. Verkhoglyadova, Jet Propulsion Laboratory, California Institute of Technology, Pasadena, CA 91109, USA.